RESEARCH ARTICLE | FEBRUARY 25 2025

Tizian Lorenzen ⊚ ; Benedikt Diederichs ⊚ ; Charles Otieno Ogolla ⊚ ; Benjamin Butz ⊚ ; Knut Müller-Caspary ➡ ⊚



Appl. Phys. Lett. 126, 081602 (2025) https://doi.org/10.1063/5.0238580





Articles You May Be Interested In

Aberration characterization of x-ray optics using multi-modal ptychography and a partially coherent source

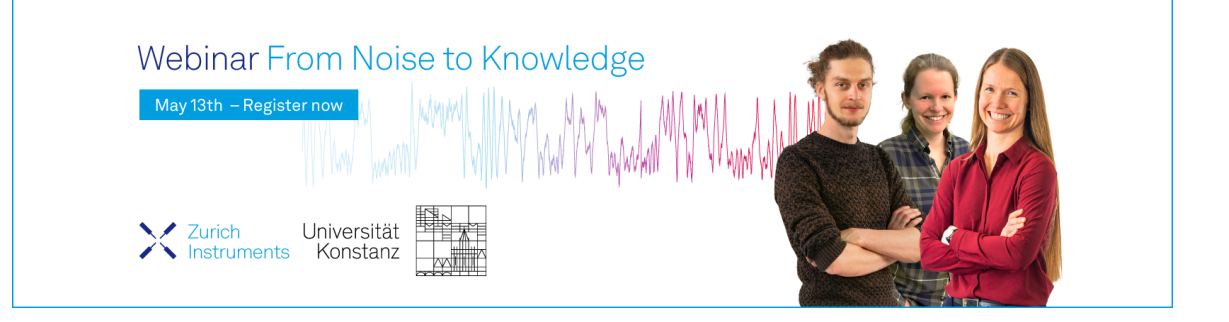
Appl. Phys. Lett. (March 2021)

Ptychography with broad-bandwidth radiation

Appl. Phys. Lett. (April 2014)

Subsampled STEM-ptychography

Appl. Phys. Lett. (July 2018)





Cite as: Appl. Phys. Lett. **126**, 081602 (2025); doi: 10.1063/5.0238580 Submitted: 12 September 2024 · Accepted: 11 February 2025 · Published Online: 25 February 2025







Tizian Lorenzen, 1 (b) Benedikt Diederichs, 1 (b) Charles Otieno Ogolla, 2 (b) Benjamin Butz, 2 (b) and Knut Müller-Caspary 1.a) (b)

AFFILIATIONS

¹Department of Chemistry and Center for NanoScience, Ludwig-Maximilians-Universität München, Butenandtstr. 11, 81377 München, Germany

ABSTRACT

Control over and knowledge of the electron probe is important in all scanning transmission electron microscopy (STEM) techniques. This is emphasized especially in electron ptychography, where the accurate probe wave function is required to deconvolve illumination from the specimen. The majority of ptychographic algorithms, such as the extended ptychographic iterative engine, reconstruct the electron probe on a pixelated grid numerically self-consistently. Solutions are thus not necessarily bound to wave functions physically realizable by the optical system. A method is presented to characterize reconstructed probes by conventional lens aberrations. The fitted aberrations are then used to investigate the quality of the retrieved probes, and their consistency is examined in a systematic study using a 4D-STEM focal series recorded for a thin SnS₂ 2D flake. Additionally, the influences of partial coherence and limited electron dose on the retrieved probes are analyzed, and the usefulness of the retrieved probes for different ptychographic methods, such as single sideband, Wigner distribution deconvolution ptychography, and gradient descent-based schemes, is elucidated. Finally, applications for ptychography-driven alignments of aberration-correcting electron optics are outlined.

© 2025 Author(s). All article content, except where otherwise noted, is licensed under a Creative Commons Attribution (CC BY) license (https://creativecommons.org/licenses/by/4.0/). https://doi.org/10.1063/5.0238580

Advances in detector hardware¹⁻⁵ and algorithmic developments^{6,7} made ptychography employing four-dimensional scanning transmission electron microscopy (4D-STEM) a powerful technique for the characterization of nanostructures, ferroelectrics, and biological molecules. 10 Ptychography offers a solution to the phase problem, which has limited both x-ray and electron microscopy since their inception. 4D-STEM involves the subsequent recording of multiple diffraction patterns at partially overlapping positions of a scanning probe. These measurements enable the retrieval of the complex object transmission function (OTF) and the wave function of the probe by electron ptychography. In addition to direct, analytical methods such as single-sideband (SSB)¹¹ and Wigner distribution deconvolution (WDD)¹² ptychography, iterative schemes such as the extended ptychographic iterative engine (ePIE)¹³ or gradient-based techniques were established, being additionally capable of deconvolving the illumination from the object blindly. 4 Given the quest for structurally and

chemically accurate object reconstructions revealing, e.g., vacancies, substitutional atoms, or valencies in 2D materials, examining the consistency of ptychographic reconstructions among different methods and their physical reliability appears expedient. In particular, the nonlinear signal formation and the complexity of the optimization problem impede a direct and compact analysis of the convergence behavior and obtained results, especially in relation to factors such as the shape of the scanning probe, the dose, partial coherence, and initialization of the reconstruction.

Here, we present a procedure to fit lens aberrations to probes retrieved unconstrained on pixelated grids using, e.g., ePIE. These aberration coefficients are then used to check the quality of the obtained reconstructions and their consistency with known models by regaining the physical parameters from the experimental setup. The retrieved aberration coefficients can then be used to electron-optically correct aberrations in automated setups. We use the retrieved

²Micro- and Nanoanalytics Group, University of Siegen, Paul-Bonatz-Str. 9-11, 57076 Siegen, Germany

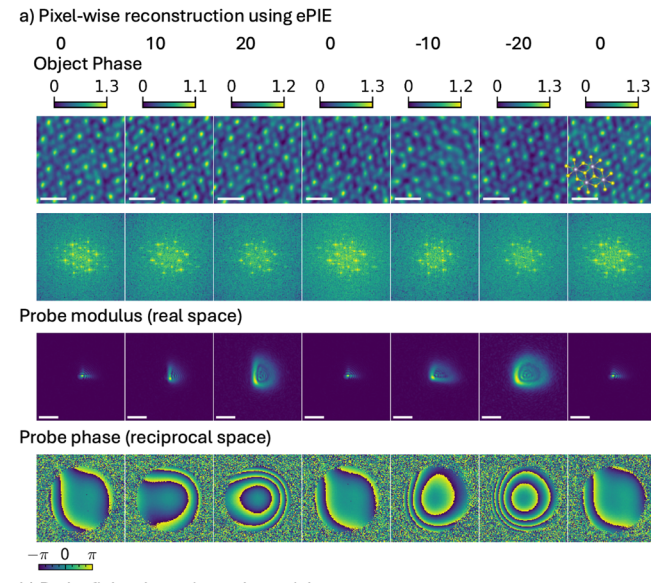
^{a)}Author to whom correspondence should be addressed: k.mueller-caspary@cup.lmu.de

aberration parameters to quantitatively compare different ptychographic models for consistency. Furthermore, the influence of partial coherence and limited electron dose on the ptychographic probes retrieved using fully coherent models, and on the fitting procedure, is investigated.

The basis for the present study is an experimental through-focus series of 4D-STEM data of a 2D SnS2 flake, acquired in a focus range of ±20 nm at a probe-corrected FEI Titan Themis (S)TEM operated at 300 kV with a semi-convergence angle of 20.4 mrad. A Medipix3 MerlinEM detector with a frame time of 420 μ s and a scan pixel size of 0.143 Å were used, the latter ensuring sufficient overlap of neighboring probe positions under in-focus conditions. An average dose of 3500 electrons was detected per diffraction pattern resulting in a total dose of approximately $1.7 \times 10^5 \,\text{Å}^{-2}$. Reconstructions were performed with a graphics processing unit (GPU)-based implementation of ePIE¹³ and gradient-based schemes employing the TorchSlice (TS) software.9 It is thus expected that ptychographic reconstructions yield (i) identical OTFs for all scans of the focal series independently of the chosen focus, and (ii) probe wave functions that only differ by Fresnel propagation, i.e., defocus. According to the electron-optical setup, probes are generally well represented by the combination of a binary aperture and a low number of axial lens aberrations (seven when considering aberrations up to the third order).

Reconstructions using ePIE are shown in Fig. 1 for the whole focal series. The in-focus data were recorded at the beginning, middle, and at end of the series to check for specimen drift, focus stability, and specimen damage. All OTF phases in Fig. 1(a) show the hexagonal structure of the SnS_2 lattice with the heavy tin columns (Z = 50) and the more weakly scattering sulfur columns (2Z = 32, see inset in Fig. 1). Importantly, the phase ranges from 0 to max. 1.3 rad are consistent among the different reconstructions, with a slight tendency to larger spans for the three in-focus datasets. In addition to specimen drift affecting the reconstruction for −10 nm defocus, the retrieved OTFs of the specimen are consistent in that specimen degradation by knock-on damage or contamination appears negligible since the three in-focus datasets yield identical results. The reconstructed probes in Fig. 1(b) show a strong contribution of coma; the probe sizes increase with the modulus of the defocus, and the curvature of the reciprocal space phase plate changes accordingly. The three in-focus probes are particularly in good agreement. To show that the defocused probe wave functions agree except for the Fresnel propagation effect, all probes have been propagated to the in-focus plane as shown in supplementary material Fig. 1. Note that the blind deconvolution yields reasonable results in all cases, since no specimen details are contained in the probe and vice versa, pointing not only to a converged ePIE but also to the specimen being thin enough such that the underlying single-scattering model is valid. However, it is also clear that partial coherence and limited electron dose affect the experimental data, and that the probes are created by a binary condenser aperture and a phase plate defined by an aberration polynomial $\chi(\vec{q})$. Consistency of the unconstrained probes from ePIE, retrieved on a pixelated grid as complex values, with electron-optical requirements is thus analyzed next.

To this end, let us consider a single probe corresponding to 4D-STEM data taken with 10 nm defocus in more detail, as shown in Fig. 2. Its amplitude is sharply peaked in real space with a coma tail extending into the upper right. The real space phase shows oscillations matching the structure of the tail. The modulus of the Fourier-



b) Probe fit by aberration polynomial Probe modulus (real space)

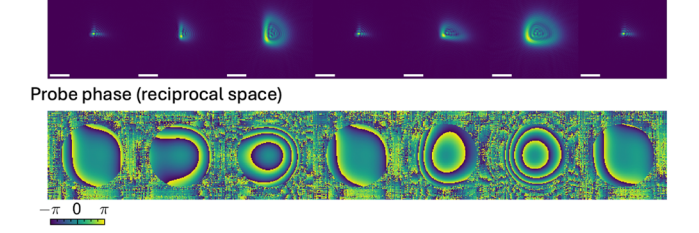


FIG. 1. Reconstructed phase gratings and probes from the 4D-STEM focal series. Phase gratings obtained using ePIE and their power spectra, reconstructed probe modulus, and reciprocal space phase plate from the experimental 4D-STEM focal series (a). The set foci are shown at the top. Modulus of the fitted probes and fitted reciprocal space phase plate (b). The real space scale bar is 5 Å in all cases. The atomic structure of tin disulfide is overlaid in the top right.

transformed probe resembles the circular condenser aperture, albeit not strictly binary and sharply terminated. This is a result of the limited electron dose in combination with partial coherence and will be discussed below. Except for a few pixels, the obtained phase plate

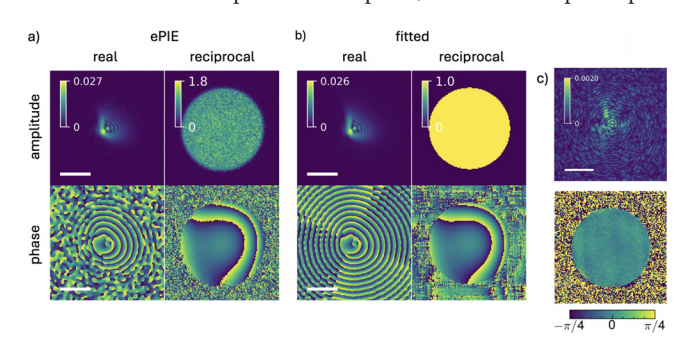


FIG. 2. Comparison of ptychographic and fitted probe. Real and reciprocal space representation of the ptychographic probe (a) and the fitted probe (b). The resulting modulus of the real space residual and the difference between the reciprocal phases are shown in (c). The real space scale bar equals 5 Å, and the aperture radius is 20.4 mrad.

(reciprocal space phase) is smooth and predominantly indicates the presence of defocus and coma from a qualitative point of view. Quantitatively, the coefficients of axial aberrations need to be determined, for which a fitting procedure to the probe wave function in Fig. 2(a) was developed. A gradient-based scheme was used to minimize the mean squared error,

$$\mathcal{L} = \sum_{i} |\psi_{\text{ePIE}}(\vec{r}_i) - \psi_{\text{fitted}}(\vec{r}_i)|^2, \tag{1}$$

between the complex ptychographic probe ψ_{ePIE} and the fitted probe ψ_{fitted} in real space. Gradients were calculated using the automatic differentiation scheme implemented in pytorch¹⁶ in combination with Adam as an optimizer.¹⁷ The fitted probe wave function ψ_{fitted} is defined as the inverse Fourier transform of a predefined aperture function $a(\vec{q})$ and a phase plate given by the aberration polynomial $\chi(\vec{q})$,

$$\psi_{\text{fitted}}(\vec{r}) = \mathscr{F}^{-1} \Big[a(\vec{q}) e^{-i\chi(\vec{q}) - 2\pi \vec{s}\vec{q}} \Big] (\vec{r}). \tag{2}$$

The vector \vec{s} takes a possible real space shift into account, which is important because the ptychographic problem is invariant with respect to real space translations. While fitting against the mean squared error of the probe intensities was performed as well, it can result in the complex conjugate wave function. The nomenclature of Haider et al. is adopted for the aberration coefficients, 15 and the fitting is restricted to third-order aberrations, as negligible improvement of the correlation coefficient and mean squared error was obtained when including higher orders. Fitting simulated probes showed the procedure being robust against additive Gaussian noise. The resulting fit is shown in Fig. 2(b). A very good match for the ptychographic probe in Fig. 2(a) is achieved resulting in a correlation coefficient of 0.99 for the amplitudes and 0.96 for the complete wave function. Additionally, the amplitude of the real space residual in Fig. 2(c) is small, reaching a maximum of 7% of the maximum probe amplitude in Fig. 2(b). Similarly, the difference between the two phase plates is mostly flat. Consequently, the ptychographic probes obtained by ePIE are well characterized using a round binary aperture and axial aberrations. The reliable description of the ptychographic probe using aberration coefficients also shows that the influence of other effects, such as the charging of the aperture edge, is minimal here.

This electron-optical parametrization was then applied to all probes retrieved from the focal series in Fig. 1(a), yielding correlation coefficients above 0.95 for the complex wave functions and 0.97 for the amplitudes. To gauge the consistency of the resulting fit with theoretical expectations for a 4D-STEM focal series, the fitted defocus $C_{1,\text{fitted}}$ was plotted against the defocus $C_{1,\text{set}}$ set at the microscope. A linear relationship,

$$C_{1,\text{fitted}} = (1.22 \pm 0.02) C_{1,\text{set}} - (2.34 \pm 0.43) \text{ nm},$$
 (3)

was found, where the low standard deviations of the linear regression support the quality of both the fitting procedure and the physical reliability of the retrieved probes. The deviation of the slope from unity is attributed to the focus calibration of the microscope. In addition to the linearity between the set and measured probe focus for the focal series in Fig. 1, an additional requirement is the stability of other aberration coefficients whose mean values and standard deviations are listed in Table I. Standard deviations amount to approximately 13 nm for the second-order aberrations and 500 nm for the third-order aberrations.

TABLE I. Average aberration coefficients and their standard deviations obtained from the focal series in Fig. 1.

Aberration	Value (nm)
A_1	2.5 ± 0.5
A_2	120 ± 12.3
B_2	257.6 ± 14.5
C_3	-653.6 ± 2116.3
S_3	86.1 ± 495.2
A_3	496.7 ± 426.4

An exception is the third-order spherical aberration C_3 for which a standard deviation of 2 μ m is obtained. The high standard deviation is a result of the fact that defocus and spherical aberration may partially compensate each other. These precisions are comparable and partly better than those obtained from Zemlin tableaus performed using an aberration corrector.

After convergence of the ePIE algorithm, the aberration coefficients are very stable. Throughout the last 12 ePIE iterations, a standard deviation below 0.05 nm was observed for the first-order aberrations, below 0.5 nm for the second-order aberrations, and below 20 nm for the third-order aberrations, with the exception of the third-order spherical aberration where higher standard deviations of up to 100 nm may be observed. A possible reason could be that defocus and spherical aberration are not orthogonal. Note that the change of the probe aberration parameters and the correlation coefficient between the fitted and ptychographic probe can be used as a criterion to judge both the convergence and physical reliability of the ptychographic reconstruction.

According to Fig. 2, the ptychographic and parametrized probes also exhibit faint differences. First, the experimental real space probe oscillations do not continue infinitely but vanish into a noise background. Second, the reciprocal space aperture is not binary as in the fitted case but shows some graininess while, furthermore, not falling exactly to zero outside the expected aperture rim. In that respect, the ePIE interaction model differs in two distinct factors from the experiment, since it assumes perfectly coherent illumination and does not include the effects of limited electron dose. ¹⁸ In the following, the influences of partially coherent illumination and limited electron dose are investigated as depicted in Fig. 3.

For that purpose, ePIE reconstructions were performed based on data simulated with the multislice algorithm assuming (i) perfect coherence, (ii) including partial temporal and spatial coherence, and (iii) including partial coherence with a dose of 3500 electrons per CBED as in the experiment. In a fully coherent simulation, ePIE retrieves the object potential and the simulated probe almost perfectly as shown in Fig. 3(a) (top left). The introduction of partial coherence suppresses the contrast of the atomic columns significantly by 25% [top right in Fig. 3(a)]. However, the influence on the retrieved probe is minimal as shown in Fig. 3(b) (top row). This is remarkable, because it means that partial coherence effects of the probe are rather considered in the retrieved OTF than in the reconstructed probe. The aperture edge in Fig. 3(c) remains sharp, and no noise background is found in real space by partial coherence effects. In contrast, the introduction of a limited dose via Poisson noise increases the agreement with the

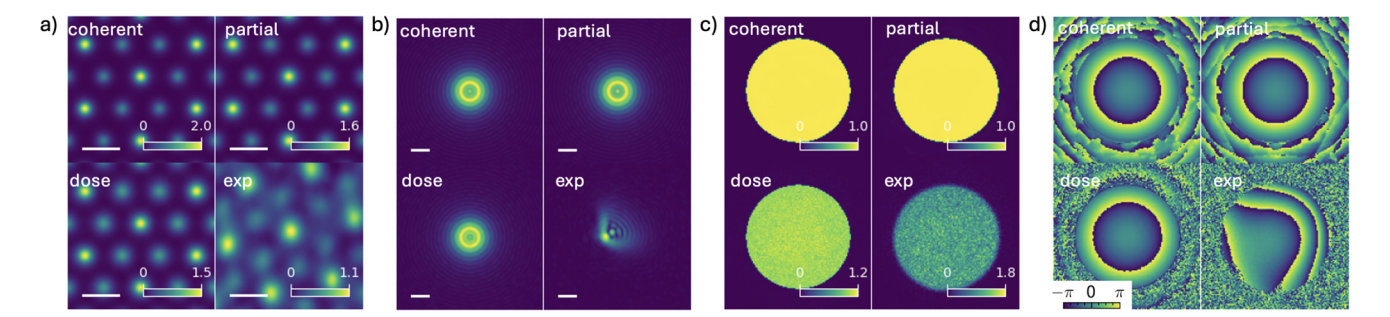


FIG. 3. Influence of partial coherence on specimen and probes retrieved using ePIE. Phase grating retrieved using ePIE for simulated data assuming perfect coherence, including the effect of partial coherence and limited electron dose (a), real space modulus, reciprocal space modulus, and reciprocal space phase of the probes retrieved in the same reconstruction (b)–(d). The results of an experimental dataset are shown as a comparison. Simulations were performed using multislice for a specimen thickness of four monolayers, standard deviations of 0.05 and 2 nm were assumed for the partial spatial and temporal coherence. The scale bar is 2 Å in all cases.

experimental results significantly, yielding the observed broadening of the atomic columns in Fig. 3(a) (bottom left). Additionally, the features noted for the experimental probe start to appear such as the graininess of the aperture in Fig. 3(c) (bottom left) and the noisy background in real space in Fig. 3(b). To conclude, the influence of the limited electron dose is significantly larger than that of the limited partial coherence in the investigated case. Importantly, the fitting procedure retrieves the correct defocus in all cases with a maximum deviation of 0.4 nm.

With the parametrized probes, it is now possible to compare different ptychographic schemes by using the measured aberration coefficients. Here, four ptychographic approaches are compared, being (i) SSB ptychography¹¹ and (ii) WDD¹² as direct inversion concepts on the one hand, as well as the iterative techniques (iii) ePIE and (iv) gradient descent-based inverse multislice using the TS software⁹ on the other hand. Note that (i)-(iii) exploit a single multiplicative interaction model using a weak phase object (SSB) or an arbitrary complex transmission function (WDD and ePIE), whereas the inverse multislice additionally takes multiple scattering into account. The results are shown in Fig. 4 for the dataset taken at +10 nm defocus. Aberrations according to Table I have been taken into account for the SSB and WDD reconstructions and used for the initialization of the inverse multislice. For the latter, partial coherence and the limited electron dose were taken into account, and the positions of the scanning probe have been optimized as well. The Poissonian loss function to include the correct maximum likelihood optimizer^{6,18} for the counting statistics has been used, and slices were optimized on a pixelated grid without constraints.

The inclusion of higher-order aberrations yields the well-resolved atomic structure in all three single-scattering ptychography techniques. The tin columns are brighter than the sulfur ones due to their higher projected potential. While SSB also shows the atomic structure with high resolution, as becomes visible in the power spectra, it exhibits significantly reduced phase contrast when compared to the other three schemes. Given the underlying weak phase object approximation, this is expected for the SSB result and indicates that the specimen violates the weak phase object approximation. In this respect, the more general interaction model exploited by WDD and ePIE yields a much better match among these reconstructions, which both show comparable phase shifts with a range being four times larger than in the SSB case. While one could argue that there is no point in performing a WDD reconstruction with a successful ePIE result already present since both

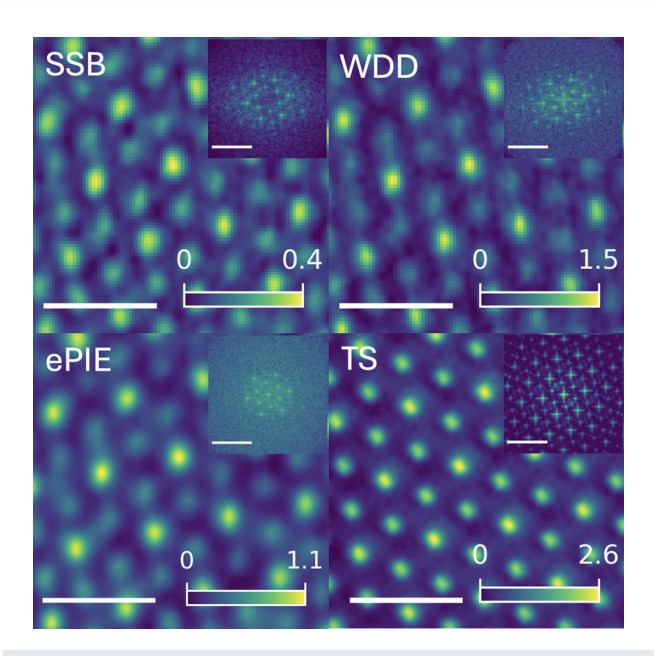


FIG. 4. Comparison of different ptychographic schemes. Reconstructed specimens and their power spectra (inset) for single-sideband (SSB) ptychography, Wigner distribution deconvolution (WDD), ePIE, and the projected potential from a TorchSlice (TS) reconstruction. The real space scale bar is $5\,\text{Å}$ in all cases, and the reciprocal space scale bar is $1\,\text{Å}^{-1}$.

algorithms are based on the same interaction model, it is to note that the phase range of the WDD reconstruction is slightly higher and that it contains higher spatial frequencies in the power spectrum that are related to the crystal lattice. This might be surprising at first glance, as the ePIE algorithm is not aperture limited in contrast to the standard implementation of the WDD reconstruction used here. However, in the present case, the resolution is mostly limited by the electron dose and as such neither of the two algorithms reach the resolution limit set by the employed aperture. The better performance of the WDD algorithm is possibly related to the direct nature of the method, which leads to the algorithm considering all diffraction patterns at once vs one at a time for ePIE, which has been reported to be more stable. On the other hand, the iterative ePIE scheme usually allows for

the robust deconvolution of the probe wave function and OTF without critical prior information and has reduced sampling requirements in scan space compared to the direct methods. Nevertheless, the deconvolution of illumination and specimen using SSB and WDD by employing aberrations obtained by parametrizing probe wave functions retrieved with ePIE is promising for the application to live reconstructions as both SSB and WDD can be formulated to be suitable for live imaging.^{22,23} Supplementary material Fig. 2 depicts a simulation study in which probes were retrieved while different effects have been taken into account in the forward simulation, such as Poisson noise, partial coherence, and scan grid distortions. Note that the focus is the most volatile parameter of the probe, whereas higher-order aberrations remain more stable in time. Performing a single ePIE reconstruction to determine higher orders, and then running live reconstructions with only the focus unknown provides thus a suitable perspective for efficient high-resolution SSB or WDD live ptychography.

We finally consider the inverse multislice reconstruction with TS bottom right in Fig. 4. Comparison of ePIE reconstructions of simulated data with the experiment showed the best agreement for four monolayers of SnS2; thus, reconstructions were performed in a fourslice model with the propagation distance matching the layer distance of 5.89 Å. The reconstructed phase grating shows strongly improved resolution with much sharper atoms and a phase spanning approximately twice the range as compared to WDD and ePIE. Aberration coefficients were found to be stable as to the initialization from the fitting procedure, except for the defocus, which was refined to be approximately 2 nm closer to the crossover of the overfocused probe. This is expected, because single-slice models (SSB, ePIE, and WDD) reveal foci within the specimen bulk, whereas multislice is capable of distinguishing between propagation of the wave function before and during the interaction with the specimen. The difference in the inverse multislice result including coherence and dose effects to the other approaches also shows that, although ePIE, SSB, and WDD accomplish a deconvolution of probe wave function and specimen and yield atomic structures at high resolution, a quantitative interpretation of the retrieved phases needs to be taken with care, even in few-layer thick sheets of 2D materials.

To conclude, using the ePIE, the interaction model of an arbitrary, multiplicative complex specimen function is less restrictive as compared to previous ptychographic aberration measurements based on the weak phase approximation.²⁴ It is found that all probes of a focal series are well characterized by aberrations and a binary aperture, only differing in focus, while all other aberrations are stable within the error margins. Other effects such as charging of apertures, partial coherence, and counting noise play a minor role in the measurements of the aberration coefficients. The determined aberrations are of significant practical use in several respects. First, they can be incorporated into other ptychographic schemes, namely SSB, WDD, and inverse multislice ptychography. Second, the retrieved aberration coefficients can be used to directly control correcting electron optics, such as stigmators or aberration correctors. While a typical ePIE reconstruction for 1282 scan pixels, including the determination of aberration coefficients, takes on the order of 1 min, being comparable to Zemlin tableau measurements of aberrations, a further advantage of ptychographybased aberration measurements is that they can be performed directly at the specimen of interest without the need for switching to a dedicated calibration sample.

See the supplementary material for all probes determined at different foci, Fresnel-propagated to the in-focus plane for comparison in Fig. 1. A simulation study according to the experimental conditions is presented in Fig. 2, demonstrating the effects of partial coherence, Poisson noise, and scan noise on probe retrieval separately.

T.L. and K.M.-C. acknowledge funding from the DFG, Contract No. EXC 2089/1-390776260 (Excellence Cluster *e-conversion*). K.M.-C. acknowledges funding from the European Research Council within the Horizon Europe innovation funding programme under Grant Agreement No. 101118656 (ERC Synergy Project No. 4D-BioSTEM).

AUTHOR DECLARATIONS Conflict of Interest

The authors have no conflicts to disclose.

Author Contributions

Tizian Lorenzen: Conceptualization (supporting); Data curation (lead); Formal analysis (lead); Investigation (lead); Methodology (equal); Software (equal); Validation (equal); Visualization (equal); Writing – original draft (equal); Writing – review & editing (supporting). Charles Otieno Ogolla: Investigation (supporting); Writing – review & editing (supporting). Benjamin Butz: Investigation (supporting); Writing – review & editing (supporting). Knut Müller-Caspary: Conceptualization (equal); Funding acquisition (equal); Methodology (equal); Project administration (lead); Resources (lead); Supervision (lead); Writing – review & editing (equal).

DATA AVAILABILITY

The data that support the findings of this study are available from the corresponding author upon reasonable request.

REFERENCES

- ¹K. Müller, H. Ryll, I. Ordavo, S. Ihle, L. Strüder, K. Volz, J. Zweck, H. Soltau, and A. Rosenauer, "Scanning transmission electron microscopy strain measurement from millisecond frames of a direct electron charge coupled device," Appl. Phys. Lett. **101**, 212110 (2012).
- ²R. Plackett, I. Horswell, E. N. Gimenez, J. Marchal, D. Omar, and N. Tartoni, "Merlin: A fast versatile readout system for Medipix3," J. Instrum. 8, C01038 (2013).
- ³M. W. Tate, P. Purohit, D. Chamberlain, K. X. Nguyen, R. Hovden, C. S. Chang, P. Deb, E. Turgut, J. T. Heron, D. G. Schlom, D. C. Ralph, G. D. Fuchs, K. S. Shanks, H. T. Philipp, D. A. Muller, and S. M. Gruner, "High dynamic range pixel array detector for scanning transmission electron microscopy," Microsc. Microanal. 22, 237–249 (2016).
- ⁴N. Denisov, D. Jannis, A. Orekhov, K. Müller-Caspary, and J. Verbeeck, "Characterisation of a Timepix detector for use in SEM acceleration voltage range," Ultramicroscopy 253, 113777 (2023).
- ⁵D. G. Stroppa, M. Meffert, C. Hoermann, P. Zambon, D. Bachevskaya, H. Remigy, C. Schulze-Briese, and L. Piazza, "From STEM to 4D STEM: Ultrafast diffraction mapping with a hybrid-pixel detector," Microsc. Today 31, 10–14 (2023).
- ⁶P. Thibault and M. Guizar-Sicairos, "Maximum-likelihood refinement for coherent diffractive imaging," New J. Phys. 14, 063004 (2012).
- ⁷Z. Chen, Y. Jiang, Y.-T. Shao, M. E. Holtz, M. Odstrčil, M. Guizar-Sicairos, I. Hanke, S. Ganschow, D. G. Schlom, and D. A. Muller, "Electron ptychography

- achieves atomic-resolution limits set by lattice vibrations," Science 372, 826–831 (2021).
- ⁸P. M. Pelz, S. M. Griffin, S. Stonemeyer, D. Popple, H. DeVyldere, P. Ercius, A. Zettl, M. C. Scott, and C. Ophus, "Solving complex nanostructures with ptychographic atomic electron tomography," Nat. Commun. 14, 7906 (2023).
- ⁹B. Diederichs, Z. Herdegen, A. Strauch, F. Filbir, and K. Müller-Caspary, "Exact inversion of partially coherent dynamical electron scattering for picometric structure retrieval," Nat. Commun. 15, 101 (2024).
- ¹⁰ B. Küçükoğlu, I. Mohammed, R. C. Guerrero-Ferreira, M. Kube, J. Radecke, S. M. Ribet, G. Varnavides, M. L. Leidl, K. Lau, S. Nazarov *et al.*, "Low-dose cryo-electron ptychography of proteins at sub-nanometer resolution," bioRxiv:2024-02 (2024).
- ¹¹J. Rodenburg, B. McCallum, and P. Nellist, "Experimental tests on double-resolution coherent imaging via STEM," Ultramicroscopy 48, 304–314 (1993).
- ¹²H. Yang, I. MacLaren, L. Jones, G. T. Martinez, M. Simson, M. Huth, H. Ryll, H. Soltau, R. Sagawa, Y. Kondo *et al.*, "Electron ptychographic phase imaging of light elements in crystalline materials using Wigner distribution deconvolution," Ultramicroscopy 180, 173–179 (2017).
- ¹³ A. M. Maiden and J. M. Rodenburg, "An improved ptychographical phase retrieval algorithm for diffractive imaging," *Ultramicroscopy* 109, 1256–1262 (2009).
- ¹⁴P. Thibault, M. Dierolf, O. Bunk, A. Menzel, and F. Pfeiffer, "Probe retrieval in ptychographic coherent diffractive imaging," *Ultramicroscopy* 109, 338–343 (2009).
- ¹⁵M. Haider, S. Uhlemann, and J. Zach, "Upper limits for the residual aberrations of a high-resolution aberration-corrected STEM," Ultramicroscopy 81, 163–175 (2000).

- ¹⁶ A. Paszke, S. Gross, F. Massa, A. Lerer, J. Bradbury, G. Chanan, T. Killeen, Z. Lin, N. Gimelshein, L. Antiga et al., "Pytorch: An imperative style, high-performance deep learning library," in Advances in Neural Information Processing Systems 32 (Curran Associates, Inc., 2019).
- ¹⁷D. P. Kingma and J. Ba, "Adam: A method for stochastic optimization," arXiv:1412.6980 (2014).
- ¹⁸M. L. Leidl, B. Diederichs, C. Sachse, and K. Müller-Caspary, "Influence of loss function and electron dose on ptychography of 2D materials using the Wirtinger flow," Micron 185, 103688 (2024).
- ¹⁹Y. Jiang, Z. Chen, Y. Han, P. Deb, H. Gao, S. Xie, P. Purohit, M. W. Tate, J. Park, S. M. Gruner *et al.*, "Electron ptychography of 2D materials to deep sub-Anström resolution." Nature 559, 343–349 (2018).
- Ångström resolution," Nature 559, 343–349 (2018).

 20 J. Rodenburg and R. Bates, "The theory of super-resolution electron microscopy via Wigner-distribution deconvolution," Philos. Trans. R. Soc. London, Ser. A 339, 521–553 (1992).
- ²¹M. Hardt and B. Recht, "Train faster, generalize better: Stability of stochastic gradient descent," in Proceedings of the 33rd International Conference on Machine Learning (2016).
- ²²A. Strauch, D. Weber, A. Clausen, A. Lesnichaia, A. Bangun, B. März, F. J. Lyu, Q. Chen, A. Rosenauer, R. Dunin-Borkowski *et al.*, "Live processing of momentum-resolved STEM data for first moment imaging and ptychography," Microsc. Microanal. 27, 1078–1092 (2021).
- ²³A. Bangun, P. F. Baumeister, A. Clausen, D. Weber, and R. E. Dunin-Borkowski, "Wigner distribution deconvolution adaptation for live ptychography reconstruction," Microsc. Microanal. 29, 994–1008 (2023).
- ²⁴H. Yang, R. Rutte, L. Jones, M. Simson, R. Sagawa, H. Ryll, M. Huth, T. Pennycook, M. Green, H. Soltau *et al.*, "Simultaneous atomic-resolution electron ptychography and z-contrast imaging of light and heavy elements in complex nanostructures," Nat. Commun. 7, 12532 (2016).